Title	Electrochemical lithium insertion behavior of combustion synthesized V2O5 cathodes for lithium-ion batteries
Author(s)	Cheah, Yan Ling; Aravindan, Vanchiappan; Madhavi, Srinivasan
Citation	Cheah, Y. L., Aravindan, V., & Madhavi, S. (2012). Electrochemical Lithium Insertion Behavior of Combustion Synthesized V2O5 Cathodes for Lithium-Ion Batteries. Journal of The Electrochemical Society, 159(3), A273-A280.
Date	2012
URL	http://hdl.handle.net/10220/10904
Rights	

Journal of The Electrochemical Society, **159** (3) A273-A280 (2012)
0013-4651/2012/159(3)/A273/8/$28.00 © The Electrochemical Society

Electrochemical Lithium Insertion Behavior of Combustion Synthesized V_2O_5 Cathodes for Lithium-Ion Batteries

Yan L. Cheah,[a] Vanchiappan Aravindan,[b] and Srinivasan Madhavi[a,b,c,z]

[a]*School of Materials Science and Engineering, Nanyang Technological University, Singapore 639798*
[b]*Energy Research Institute @ NTU (ERI@N) and* [c]*TUM-CREATE Center for Electromobility, Nanyang Technological University, Singapore 637553*

Sub-micron size vanadium pentoxide (V_2O_5) particles are synthesized by novel urea assisted combustion method. Comprehensive characterization and electrochemical studies related to sintering temperature and duration are presented. X-ray diffraction (XRD) patterns showed the formation of pure-phase V_2O_5 and the surface morphologies are studied by field emission scanning electron microscopy (FE-SEM). Electrochemical properties of the sintered V_2O_5 as a cathode in lithium-ion batteries are explored with respect to synthesis parameters using cyclic voltammetry and galvanostatic charge-discharge studies. The V_2O_5 particles obtained from 600°C sintering temperature for 1 h exhibits a higher initial discharge capacity ~320 mAh g^{-1} (~2.2 Li per V_2O_5) between 1.75–4.0 V *vs.* Li/Li^+ at 0.1 C rate and shows good capacity retention of >70% after 50 cycles. Electrochemical impedance spectroscopy (EIS) studies show that the urea combustion method enables increased Li^+ ion diffusion pathways and electro-active surface area in V_2O_5 particles. Ball milling procedure with or without carbon is also adopted to further reduce the particle size of V_2O_5 and related electrochemical properties are evaluated and described.
 [DOI: 10.1149/2.071203jes]

Manuscript submitted October 10, 2011; revised manuscript received December 6, 2011. Published January 10, 2012.

Lithium-ion batteries (LIB) are becoming one of the promising and attractive energy storage systems for electric vehicle (EV), hybrid and plug-in hybrid electric vehicle (HEV/P-HEV) applications.[1–5] Commercial LIB comprises $LiCoO_2$ cathode and it is capable of delivering maximum capacity of ~140 mAh g^{-1} corresponding to utilization of only 50% active material ($Li_{0.5}CoO_2$). Moreover, its poor thermal stability and high material costs impede their potential use in large-scale applications. As a result, other candidate cathode chemistries such as olivine ($LiFePO_4$), spinel ($LiMn_2O_4$) and $LiNi_{1/3}Mn_{1/3}Co_{1/3}O_2$ are also extensively investigated as possible alternative to $LiCoO_2$ for EV/HEV applications. For example, spinel $LiMn_2O_4$ suffers from severe Mn^{3+} dissolution problem which attacks the counter electrode leading to degradation in electrochemical cell performance. Although $LiFePO_4$ is commercialized by few industries, but still it suffers the poor conducting issues and also restricted by the lower operating potential. The layered $LiNi_{1/3}Mn_{1/3}Co_{1/3}O_2$, originally introduced by Ozhuku et al. (2001),[6] exhibits high capacity, structural and thermal stability, and excellent cycling behavior. Yet, there exists, still, many issues to be addressed, such as low rate capability, considerable capacity loss during high current rates. In addition all the aforementioned cathode materials are capable of delivering discharge capacity less than 200 mAh g^{-1}. Hence, the search for high capacity cathodes is ongoing to power the high energy density LIB power packs for future EV/HEV applications.

Vanadium pentoxide (V_2O_5)[7,8] is an attractive cathode material for high energy density LIBs. Due to its layered structure, the insertion up to ~3 mol. Li^+ ion per formula unit ($V_2O_5 + xLi^+ + xe^- \leftrightarrow Li_xV_2O_5$) which leads to higher theoretical capacity of ~400 mAh g^{-1}.[38,51] V_2O_5 also has the advantages of low cost and abundant sources on the earth crust. However, problems such as severe capacity fading and poor rate capability prevent its use in commercial LIBs. Possibly, sluggish Li diffusion behavior, structural instability with lithium intercalation/de-intercalation and low electronic conductivity (10^{-2}–10^{-3} S cm^{-1}) are main cause for such fading. Several approaches have been adopted to circumvent the aforementioned issues, such as modifying the crystal structure[9–11] to improve the Li^+ ion diffusion by creating more open structures,[14,20] surface modification by conductive additives[15,17,18] and patterning the one dimensional nanostructures.[12–14,16,19,20] As a result, research focus has been progressively moved away from bulk V_2O_5 particles.[21–24] On the contrary, here an attempt has been made to synthesize sub-micron size V_2O_5 particles via urea assisted combustion technique by controlling various parameters to achieve high performance material. Further, we believe that, it is possible to achieve high specific capacity and also increase the cyclic stability of the V_2O_5 cathode using such sub-micron size particles by this route. The performance of V_2O_5 materials reported by other synthesis techniques are compared and given in Table I.

Urea combustion is a low temperature, relatively simple, cost effective and convenient method to obtain the materials with high yield. It involves exothermic reaction between urea (fuel) and nitrates (oxidizer) which drives the chemical synthesis.[25,26] Due to the self-propagating effect of this exothermic reaction, it enables the reaction to occur spontaneously at relatively lower temperatures leading to the formation of metal oxides thereby liberating nitrogen, hydrogen and oxygen gases.[27] It is well known that the electrochemical behavior of cathode materials strongly depends on the synthesis route, morphology and particle size (Table I). In this paper, the synthesis of V_2O_5 using urea assisted combustion is optimized and then a correlation between synthesis parameters including sintering temperatures, sintering time, ball milling with or without carbon on the electrochemical lithium intercalation have been studied and described in detail.

Experimental

V_2O_5 synthesis and characterization.— Vanadyl acetylacetonate ($VO(acac)_2$, 98%, Sigma-Aldrich, 2.65 g) was dissolved in nitric acid (69%, Honeywell, 5 mL) by heating at 60°C with continuous stirring resulting in a blue colored solution to which urea (Panreac, 1.8 g) was added until dissolution occurred. This mixture was heated at 300°C for 20 min to enable self-propagating combustion reaction. The obtained powder comprising the mixture of ~55 wt% V_2O_5 and ~46 wt% VO_2 in the crystalline phase (as confirmed by Rietveld refinement via Topas V3 software), as well as ~20 wt% amorphous carbon. Hence, a subsequent heat-treatment is required to achieve highly crystalline and single phase V_2O_5 particles. The powder obtained from the combustion was sintered at various temperatures (300–600°C) for different durations ranging from 1–3 h in air to obtain single-phase V_2O_5. For comparison, V_2O_5 was also prepared by direct heating of 2.65 g of $VO(acac.)_2$ at 600°C for 1 h without any combustion process. In addition, heat-treated (600°C sintered for 1 h) powder was ball-milled for further size reduction using high energy ball-mill (Spex, 8000D) for 1 h with and without carbon. For ball milling with carbon, active material to carbon ratio of 3:1 was maintained and no more carbon was included during the fabrication of the electrode.

Morphological features of sintered V_2O_5 powders were studied using field emission scanning electron microscope (FE-SEM, JEOL

[z] E-mail: Madhavi@ntu.edu.sg

Table I. Electrochemical performance of various V_2O_5 morphologies reported in literature.

Morphology	Synthesis method	Initial discharge capacity (mAh g^{-1}) at 0.1C	Capacity at n^{th} cycle (mAh g^{-1}) at 0.1C	Crystal size (nm)	Diameter (nm)	BET surface area (m^2 g^{-1})	Ref.
Nanofibers	Electrospinning	375	347 (20^{th})	15.5	350	97	44
Nanofibers	Electrospinning	316	220 (20^{th})	70–80	500–1200	NA	20
Microspheres	Hydrolysis	437	245 (20^{th})	NA	NA	31.2	45
Nanorod	Thermal decomposition	266	240 (30^{th})	48	NA	NA	38
Nanowires	Electrospinning	390	201 (50^{th})	50	200–250	NA	14
Nanocomposite (PANI)	Hydrothermal	239	209 (30^{th})	10–40	NA	NA	46
Thin film	E-beam irradiation	343	NA	NA	NA	NA	47
Nanowires	Hydrothermal	351	NA	NA	80–120	NA	8
Nanorods	Annealing	260	260 (50^{th})	7–35	NA	NA	13
Nanofibers	Electrospinning	360	240 (25^{th})	NA	40–70	NA	12
Submicron belts	Sol-gel	346	240 (20^{th})	NA	NA	NA	19
Nanoscale single crystal	Electrospinning	120	NA	NA	250	NA	48
Nanostrips	Polyol	300	80 (20^{th})	NA	NA	NA	16
Nanorods	Melt quenching	385	230 (50^{th})	NA	10–50	NA	17
Microspheres	Solution method	319	160 (45^{th})	NA	NA	NA	49
Nanowires	Hydrothermal	327	NA	NA	NA	NA	50
Nanopowder	Urea combustion	320	230 (50^{th})	200	NA	3	Current work

JSM-7600F) with an accelerating voltage of 5 kV and a transmission electron microscope (TEM, JEOL 2100F) in high resolution mode operating at 200 kV. Structural properties of V_2O_5 powders were examined using Bruker X-ray diffractometer using Cu-Kα radiation between 10 to 80°. The obtained X-ray diffraction (XRD) patterns were analyzed by Rietveld refinement[28,29] within the software Topas V3 (Bruker-AXS), using fundamental parameters approach.[30] Thermo-gravimetric analysis (TGA) of the as-combustion synthesized powder was recorded using Perkin Elmer Q500 with the scan rate of 5°C min^{-1} from room temperature to 850°C. Fourier transform infrared spectroscopy (FT-IR) was recorded on KBr pellets of sintered V_2O_5 powders using a Perkin Elmer Spectrum GX FT-IR in the range of 4000 to 400 cm^{-1}. Brunauer-Emmet-Teller (BET) surface area studies were also conducted using Nova 3200e surface area and porosity analyser.

Electrode fabrication process.— The composite cathodes were prepared by mixing active material (V_2O_5), binder (Kynar 2801), and conductive additive (Super P Li carbon, Timcal) in the weight ratio 60:20:20, respectively, using 1-methyl-2-pyrrolidinone (NMP, Sigma-Aldrich) solvent for binder to form slurry. The resulting viscous slurry was stirred continuously and subsequently coated on aluminum foil (Hohsen Corporation) using a doctor blade. The slurry-coated Al foils were dried in a vacuum oven for several hours to remove the solvent molecules and pressed in between the twin roller to provide good adherence toward current collector. Then the dried composite V_2O_5 electrodes were punched out with 16 mm diameter blanks and same area of lithium foil (∼ 0.59 mm thick, Hohsen Corporation, Japan) was used as the counter electrode. The lithium intercalation properties were studied in half-cell configuration using CR 2016 coin cells assembled in an Argon-filled glove box (MBraun). The 1 M $LiPF_6$ in ethylene carbonate (EC): diethyl carbonate (DEC) (1:1 wt%, Danvec) binary mixture was used as electrolyte and separated by Celgard 2400.

Galvanostatic discharge-charge cycling was carried out at room temperature using battery tester systems (Neware). Cyclic voltammetry (CV) studies were conducted in the same two electrode configuration at the scan rate of 0.1 mV s^{-1}, in which metallic lithium act as counter and reference electrode. Both CV and electrochemical impedance spectroscopic (EIS) studies were conducted using Solartron, 1470E and SI 1255B Impedance/gain-phase analyzer coupled with a potentiostat. EIS studies were carried out on equilibrated cells before cycling, by applying a.c. amplitude of 10 mV over the frequency range 100 kHz to 5 mHz at open circuit potential, at room temperature. The Nyquist plots Z″ vs. Z′ were derived and analyzed using Zplot and Zview software (Version 2.2, Scribner Associates Inc., USA).

Results and Discussion

Morphological and compositional studies.— FE-SEM recorded on V_2O_5 powder sintered at 600°C for 1 h in air (Figure 1a) revealed irregular shape V_2O_5 particle morphology with size ranging from 200-800 nm. The TEM image in Figure 1b shows the formation of well crystalline V_2O_5 particle and it was confirmed by SAED patterns. The observed diffraction spots of the crystal can be indexed to the (410) and (110) planes of the planes of the Shcherbinaite V_2O_5 phase.

A representative X-ray powder diffraction (XRD) pattern evaluated by Rietveld refinement is presented in Figure 2a. The family of XRD patterns of sintered V_2O_5 powders are collected and presented in Figure 2b. Herein, the following labeling system has been used to describe the synthesized V_2O_5 powders, for example, VUC 600-1 here, VUC represents V_2O_5 by urea combustion, sintered at 600°C for duration of 1h. Rietveld refinements are carried out for all the powders prepared using TOPAS software. Observed reflections indicate the formation of single phase orthorhombic V_2O_5 corresponding to the layered Shcherbinaite structure ($Pmn2_1$), without any impurity phases. Calculated lattice parameters and crystallite sizes obtained from Scherrer equation are presented in Figure 3a-3c and 3d, respectively. It is worth to mention that, increasing sintering temperature results increase of lattice parameter values. Such increasing trends are also observed while increasing sintering time as well. Nevertheless, the observed values for lattice parameters a and c are slightly less than the literature values (JCPDS 89-2482 a = 11.544(2) Å, b = 4.383 (1) Å and c = 3.571 (1) Å) given in the corresponding Figures 3a–3c, whereas the lattice parameter b value is slightly higher than reported. Furthermore, increasing the sintering temperature from 300–600°C leads to a nearly exponential increase in crystallite size and it is clearly seen from Figure 3d. Overall increase in sintering duration (for example, 2 or 3 h) reveals noticeable increase in lattice parameter values and this effect is also more pronounced at higher sintering temperatures (400, 500 and 600°C). Also, higher sintering temperature leads to increase in crystallite size, as given in Figure 3d. As the crystallite sizes obtained from the refinement data are much smaller than that observed from FE-SEM analysis and it is possible reason that the agglomeration of the crystallites may have occurred. The crystallite sizes are compared with V_2O_5 particles obtained at

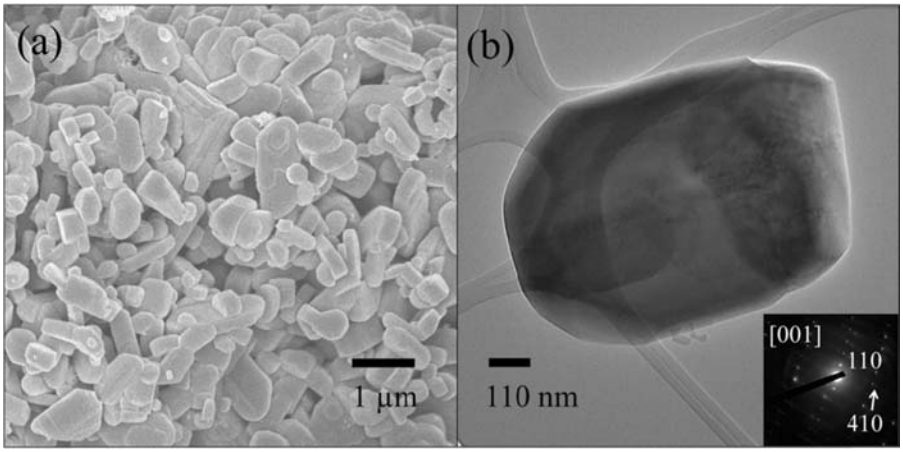

Figure 1. (a) Field emission secondary electron image (FE-SEM) and (b) transmission electron microscope (TEM) image with indexed selected area electron diffraction pattern (SAED) (inset) of VUC 600-1.

600°C for 1 h and subsequently ball-milled for 1 h. Crystallite sizes of the ball-milled particles are reduced from 200 to 20 nm. At the same time, when the particles are ball-milled with conducting carbon (3:1 w/w), the average crystallite sizes are further reduced from 200 to 28 nm.

It is known that the detection of residual organic molecules in V_2O_5 particles by XRD analysis is complicated. Hence, thermogravimetric studies are carried out and presented in Figure 4a. Noticeable amount of (∼20 wt%) weight loss is observed from the TGA of the as-combustion synthesized powder around 400°C. This weight loss is an indication of the complete phase transformation from VO_2 to V_2O_5 occurs during sintering >400°C in air.[38] In order to confirm the formation of organic-moieties-free V_2O_5 powders, FT-IR spectra has been recorded for all the powders and selectively presented in Figure 4b. All the recorded FT-IR spectra of V_2O_5 comprise three characteristic bands at 1009, 817 and 527 cm^{-1}, irrespective of the sintering temperature. The sharp peak around 1009 cm^{-1} corresponds to the V=O stretching vibration and broad peaks at 827 and 527 cm^{-1} are assigned to asymmetric and symmetric stretching modes of V-O-V bonds respectively.[31,32] Few additional peaks are observed in the case of 300°C sintered materials for all durations. The peaks around 1392, 1612 and 1717 cm^{-1} are related to the presence of urea, as well as O–H bond vibrations.[33–35] This clearly indicates that the urea is not fully decomposed during the sintering process at 300°C, whereas

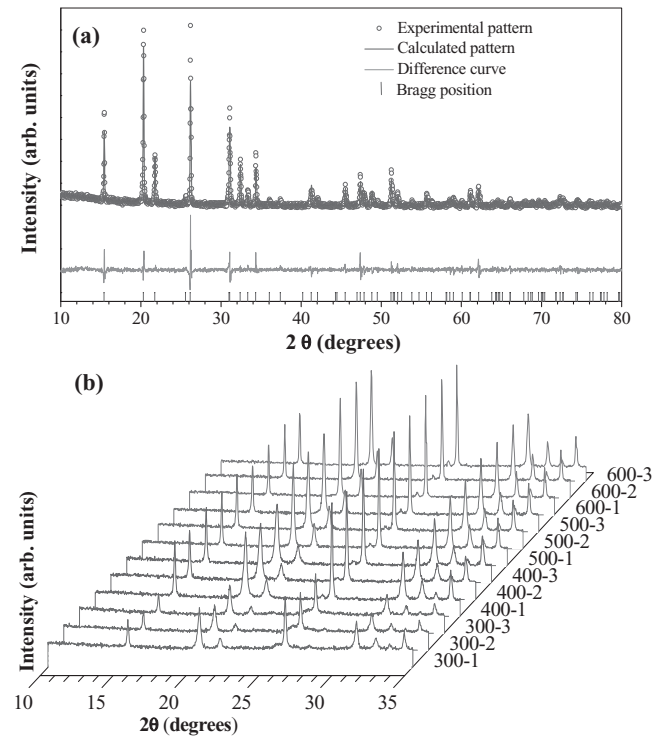

Figure 2. (a) Rietveld refined XRD pattern of V_2O_5 prepared at 600°C for 1 h and (b) family of XRD patterns of all samples sintered at 300, 400, 500 and 600°C for durations of 1, 2 and 3 h respectively.

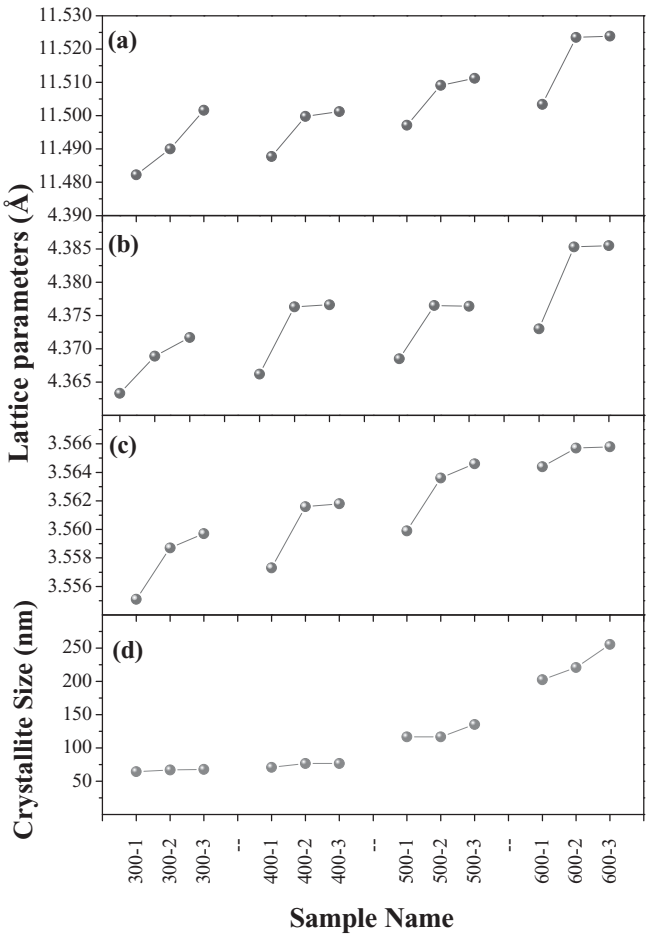

Figure 3. Rietveld refinement parameter values (a), (b), (c) Lattice parameters, and (d) crystal sizes of all samples sintered at 300, 400, 500 and 600°C for durations of 1, 2 and 3 h respectively.

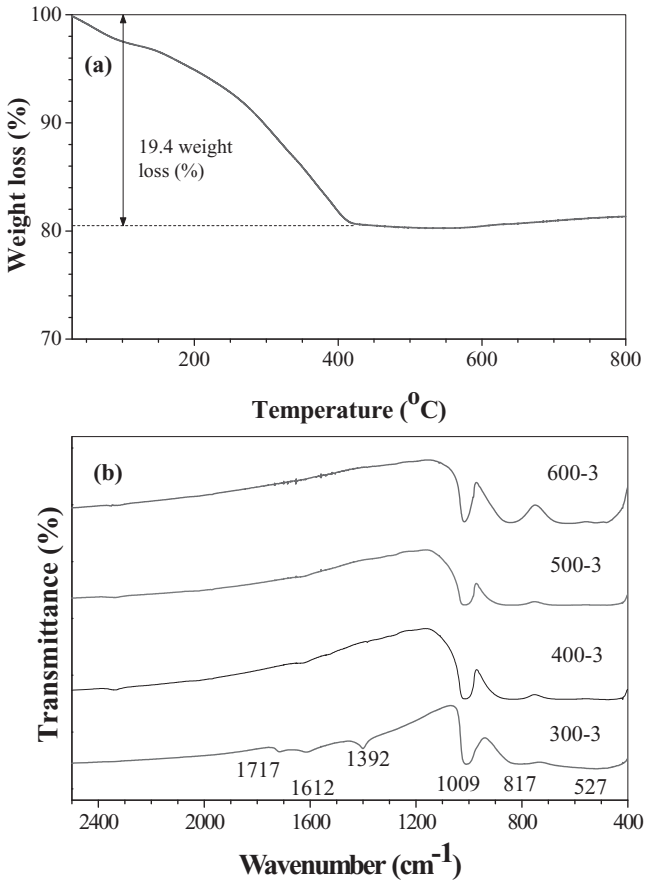

Figure 4. Fourier-transform infrared spectra (FT-IR) of samples sintered at 300, 400, 500 and 600°C for 3 h respectively.

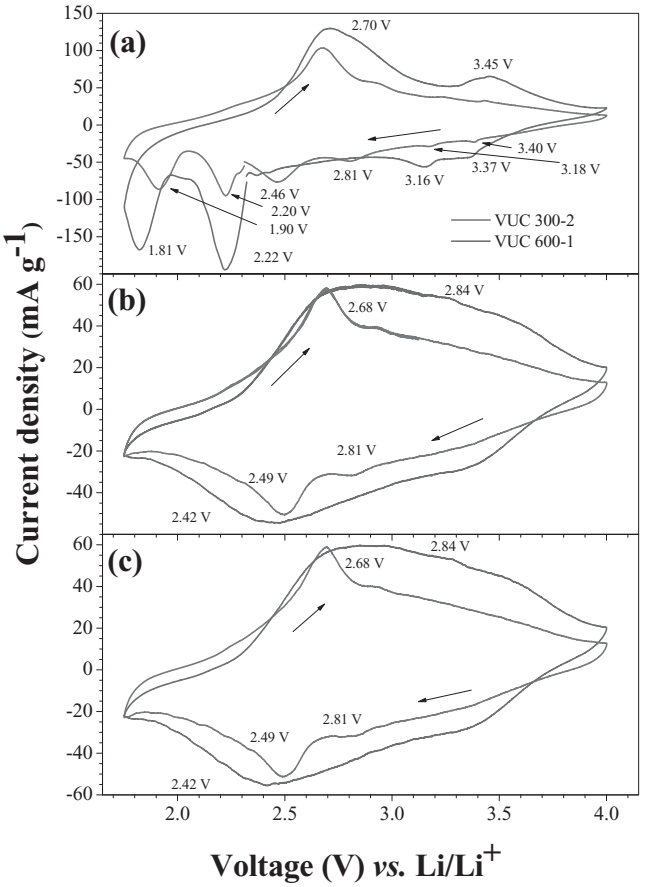

Figure 5. Cyclic voltammograms of VUC 300-2 and VUC 600-1 showing (a) first cycle, (b) second cycle and (c) 20th cycle, in which metallic lithium serves as both counter and reference electrodes in two electrode coin cell configuration with the scan rate of 0.1 mV s^{-1} between 1.75–4.0 V *vs.* Li/Li^+.

there is no such peaks are observed in the samples heat treated at 400, 500 and 600°C for all durations indicating the complete degradation of organic molecules. Hence, it can be concluded that high purity V_2O_5 particles could be obtained the sintering temperature above 300°C. The observed FT-IR spectrum is in good agreement with TGA observations.

BET surface area analysis of the synthesized V_2O_5 powders are investigated and presented. The V_2O_5 obtained from the sintering temperatures of 600 and 500°C for 1–3 h exhibiting lowest surface area (~3 m^2 g^{-1}) of the materials prepared. However, sintering the materials at 400°C gives rise to higher surface area of 6–8 m^2 g^{-1} whereas those prepared at 300°C showed highest surface area of 6–11 m^2 g^{-1}. As expected, the ballmilling procedure with carbon yielded slightly higher surface area for V_2O_5 particles of 19 m^2 g^{-1}.

Electrochemical studies.— Electrochemical properties of the synthesized V_2O_5 particles are evaluated by means of galvanostatic and potentiostatic modes in half-cell (Li/V_2O_5) configuration. All the half-cells are cycled between 1.75–4.0 V at 0.1 C in room temperature conditions by galvanostatically. As described in our previous work,[20] the insertion of lithium ions into V_2O_5 layers results the phase transformation of V_2O_5 to $Li_xV_2O_5$ leading to distortion in layered structure due to the occupancy of Li^+ ions into the spaces between the layers of VO_5 octahedral unit. The galvanostatic cycling studies are carried out for all the temperature conditions and sintering durations at 0.1 C rate and we are presenting the best performing materials in each sintering temperature. The V_2O_5 powders obtained from sintering at 600°C for 1 h showed best cycling performance, whereas material sintered at 300°C for 2 h (VUC 300-2) presented a poor performance among the materials prepared in this work. The detailed analysis will be discussed in later sections.

Cyclic voltammograms (CV) of Li/V_2O_5 cells (VUC 600-1 and VUC 300-2) are collected in the range of 1.75–4.0 V *vs.* Li/Li^+ at the slow scan rate of 0.1 mV s^{-1} to understand the phase transformation occurring during lithium intercalation/de-intercalation into VO_5 layers and presented in Figure 5. The following equation indicates the typical intercalation mechanism in V_2O_5 matrix,

$$V_2O_5 + xLi^+ + xe^- \leftrightarrow Li_xV_2O_5 \quad [1]$$

The Li/V_2O_5 cells are first discharged to intercalate the Li^+ ions in to V_2O_5 lattice. In the 1st cycle (Fig. 5a), several oxidation/reduction peaks are observed for both VUC 600-1 and VUC 300-2 powders and corresponding to the intercalation/de-intercalation processes of Li^+ in V_2O_5. The reduction (cathodic) peaks are observed at ~3.37, ~3.16, ~2.22, and ~1.81 V *vs.* Li/Li^+, whereas two oxidation peaks only observed at ~2.70 and ~3.45 V *vs.* Li/Li^+, respectively in both materials with different current densities. This variation in the current density may attribute to the nature of crystallinity of materials synthesized. The appearance of cathodic peaks indicates that the reduction of V^{5+} in V_2O_5 takes place as a multistep process within the voltage range 1.75 to 4.0 V.[20] The cathodic peaks at ~3.37 and ~3.16 V indicates the reduction of V^{5+} to V^{4+}, leads to the formation of ε-$Li_xV_2O_5$ phase. The other cathodic peaks ~2.22 and ~1.81 V belongs to partial reduction of V^{4+} to V^{3+} and this reduction reveal the formation of δ- and ε-$Li_xV_2O_5$ mixed phases. Cycling below 2.0 V *vs.* Li/Li^+ leads to the formation of irreversible ε-$Li_xV_2O_5$ phase which is confirmed by the appearance of reduction peak at ~1.81 V.[20] This reduction process enables the accommodation of more than 2 Li per

V_2O_5 formula unit. However, reversible reactions are takes place only in the potentials at ~2.70 and ~3.45 V *vs.* Li/Li$^+$ during anodic scan.

During subsequent cycles (Figure 5b & 5c), only one main well-defined oxidation/reduction pair is present for VUC 600-1. Further, the reduction peak is shifted to ~2.42 V, whereas oxidation peak remains at ~2.84 V *vs.* Li/Li$^+$. These peaks are intact upon further cycling to 20 cycles, indicating the reversibility of the redox reactions. Whereas, the CV of VUC 300-2 is concerned, in the first cycle, it also undergoes similar reduction (cathodic) process of VUC 600-1 and exhibiting characteristic potentials at ~3.4, ~3.18, ~2.2 and ~1.9 V *vs.* Li/Li$^+$ respectively. In addition to above, two more additional reduction peaks can be observed at ~2.46 and ~2.81 V. These extra peaks can be attributed to the unwanted side reactions of organic impurities present in the VUC 300-2 sample. However, it shows the prominent oxidation peak at ~2.68 V in the first cycle rather than VUC 600-1. In the subsequent cycles (Figure 5b & 5c), two reduction peaks remains at ~2.49 and ~2.81 V *vs.* Li/Li$^+$. The difference in the oxidation peaks of VUC 300-2 (~2.68 V) and VUC 600-1 (~2.84 V) in subsequent cycles may also be attributed to the incomplete formation of crystalline V_2O_5 phase, which provides sluggish kinetics during insertion/extraction of Li$^+$ ions results slight shift in the potentials. At the same time, organic impurities present in VUC 300-2 cannot be ruled out.

The galvanostatic cycling profiles of VUC 600-1 and VUC 300-2 coin cells cycled between 1.75– 4.0 V *vs.* Li/Li$^+$ at 0.1 C rate (or 35 mA g^{-1}) at room temperature are shown in Figure 6. Both samples show multiple plateaus during first discharge, which is consistent with the CV analysis and data reported elsewhere.[12,14,16,36] Such plateaus are more prominent in the VUC 600-1 cell when compared to VUC 300-2 (Figure 6a). The first discharge plateau occurs at 3.18 V vs. Li/Li$^+$ this can be correlated to the reduction of V^{5+} to V^{4+} to enable the intercalation of Li into the layered V_2O_5. As a result, a mixture of α+ε-Li$_x$V$_2$O$_5$ phases are formed (eqn. 2).[13,22,37] Upon further discharge, two stable plateaus at ~2.24 and ~1.90 V are observed. The plateau at ~2.24 V is an indication of the formation of δ-Li$_x$V$_2$O$_5$ and further V^{4+} is partially reduced to V^{3+} forming the δ- and ε-Li$_x$V$_2$O$_5$ mixed phase. The plateau ~1.9 V is believed to be the transformation of δ- Li$_x$V$_2$O$_5$ to ε-Li$_x$V$_2$O$_5$ phase. Further discharging into 1.75 V causes the irreversible formation of ε-Li$_x$V$_2$O$_5$ and this holds good agreement with reduction potential in the CV ~1.81 V *vs.* Li/Li$^+$.

In the case of VUC 300-2, the first discharge profile plateaus are not prominent when compared to VUC 600-1, which can be attributed to the incomplete crystallization of V_2O_5, thereby preventing the faster diffusion of Li$^+$ ions and presence of impurities cannot be excluded (Figure 6b). In turn, incomplete reduction of V^{5+} to V^{4+} and V^{3+} takes place which leads to considerably less initial discharge capacity (250 mAh g^{-1}) when compared to VUC 600-1 at 0.1 C (320 mAh g^{-1}).[13,22] In subsequent cycles, plateaus are not prominent in both cases and exhibiting the monotonous charge and discharge curves, which indicates that the Li$^+$ intercalation/de-intercalation occurred reversibly in mixed phases of Li$_x$V$_2$O$_5$ formed after the first discharge. The specific discharge capacities of 320 and 250 mAh g^{-1} are obtained for first and second cycles, respectively for VUC 600-1. The VUC 300-2 delivered the discharge capacities of 250 and 240 mAh g^{-1} for first and second cycle. This improved capacity retention of VUC 300-2 rather VUC 600-1 is ascribed to the incomplete formation of Li$_x$V$_2$O$_5$ phases. As expected, highly crystalline phase V_2O_5 (VUC 600-1) experiences large irreversible capacity loss, which is similar to the previous reports on the V_2O_5 system.[8,12–14,16,19,20,39,47]

As mentioned earlier, all V_2O_5 powders obtained using urea combustion synthesis were cycled galvanostatically at 0.1 C rate (35 mA g^{-1}) and presented in Figure 7. Other than VUC 600-1 and VUC 300-2, the cycling performance of other samples VUC 400-3 (sintered at 400°C for 3 h) and VUC 500-1 (sintered at 500°C for 1 h)

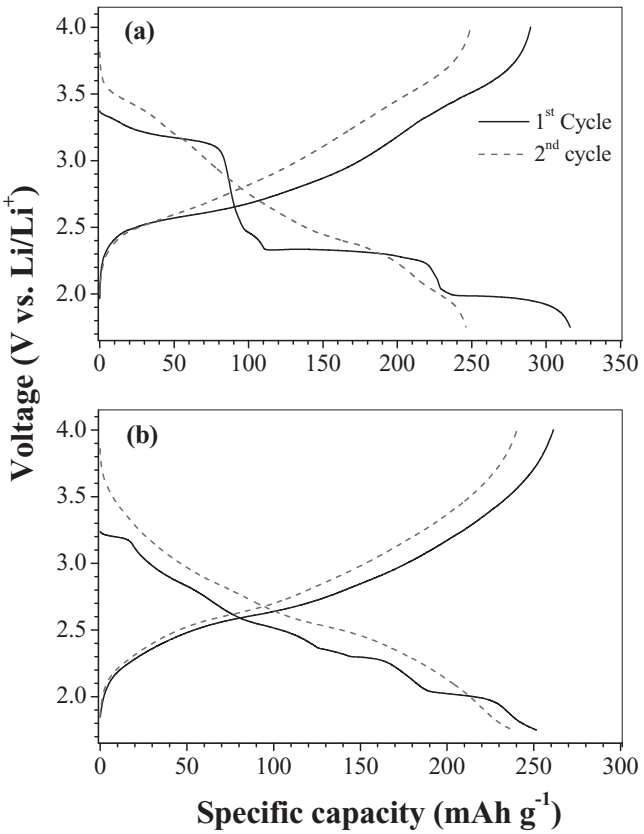

Figure 6. Typical galvanostatic cycles showing first and second charge and discharge curves of (a) VUC 600-1 and (b) VUC 300-2 cells between 1.75–4.0 V *vs.* Li/Li$^+$ at 0.1 C rate.

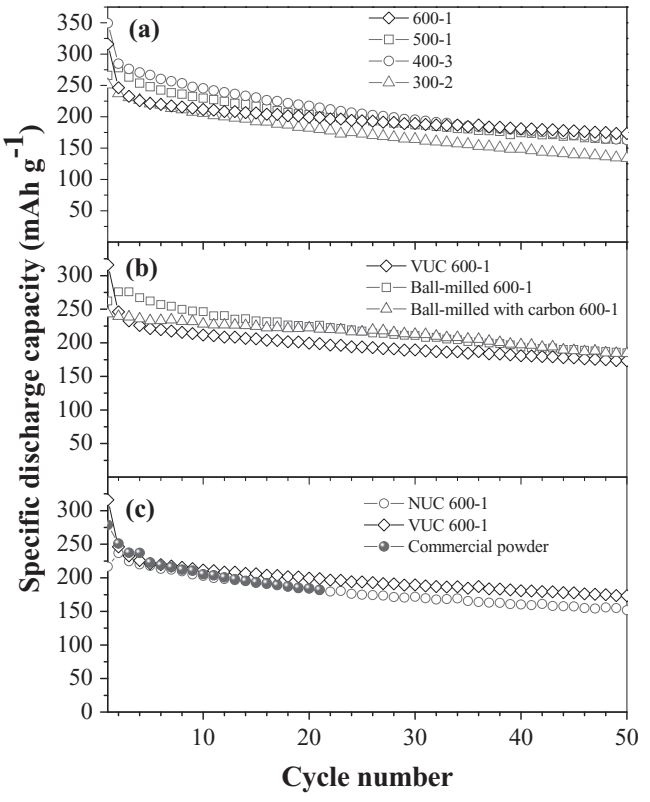

Figure 7. Plot of specific discharge capacity *vs.* cycle number (a) VUC 600-1, 500-1, 400-3 and 300-2, (b) VUC 600-1, ball-milled VUC 600-1 and ball-milled VUC 600-1 with carbon, and (c) VUC 600-1, NUC 600-1 (non-combustion synthesized) and commercial V_2O_5 powder.

are also presented in Figure 7a. The powder VUC 600-1 delivered initial specific discharge capacity of 320 mAh g^{-1} and maintains stable discharge capacity of ~230 mAh g^{-1} (72% of initial discharge capacity) after 50 cycles. Such initial specific capacity is comparable than those reported in literature[14,16,38] especially for one-dimensional nanostructures, as given in Table I. Despite the relatively lower BET surface area, VUC 600-1 has comparable initial discharge capacity to 1D nanostructures, and along with much improved cyclic retention properties.

On the other hand, VUC 500-1 presented an initial specific discharge capacity of 270 mAh g^{-1} and 59% of its initial discharge capacity only retained after 50 cycles. Similarly, VUC 400-3, 300-2 exhibited initial specific discharge capacity of 350 and 250 mAh g^{-1}, respectively. The capacity retention of VUC 400-3 and 300-2 is found to be 49 and 50% respectively after 50 cycles.

In order to study the effect of particle size on the electrochemical properties V_2O_5 powders, the VUC 600-1 is subsequently ball-milled using high energy milling with or without carbon. The cycling performance of the ball milled and native V_2O_5 are illustrated in Figure 7b. The ball-milled powder showed slightly lower initial discharge capacity of 260 mAh g^{-1} than the native compound, but an improved cyclic retention of 77% after 50 cycles is noted. Similarly, the powder, which is ball-milled with conductive carbon showed initial capacity of 245 mAh g^{-1} and better capacity retention of 82% is observed after 50 cycles than rest of its counterparts and this result is expected. Apart from the size reduction, ballmilling with carbon particles provides enhanced contact toward active material particulates than conventional mixing and thereby improving the performance of the cell. The powder morphology of the sample enables further improvement of cycling stability by a simple ballmilling procedure, which is not possible for other nanostructures as mentioned in Table I, as the morphology would be destroyed.

Furthermore, the role of combustion synthesis on the performance of V_2O_5 is compared by direct sintering of the starting material at 600°C for 1 h (Non-Urea Combustion, NUC 600-1). The electrochemical properties of above material was evaluated and compared with VUC 600-1 and commercially available material. The NUC 600-1 cell delivered the lower initial discharge capacity of 220 mAh g^{-1} when compared to 320 and 278 mAh g^{-1} for VUC 600-1 and commercial powders, respectively. The capacity retention of VUC 600-1 and NUC 600-1 powders are almost same ~71% after 50 cycles. However, the urea combustion synthesis leads to slightly increased initial discharge capacity than rest.

Based on the electrochemical performance of V_2O_5 particles prepared by various conditions as stated above, the VUC 600-1 powder rendered better electrochemical performance among the samples tested. The same material has been subjected to rate performance studies with different C-rates conducted between 1.75 to 4.0 V and presented in Figure 8 with two duplicate cells. In both cells, it is evident that specific discharge capacity tends to decreases slowly at low current rate (0.1 C) during prolonged cycling. However, capacity fading is significantly improved when the cells are cycled at high currents, for example 0.5 or 1 or 2 C-rates. For the rate performance studies, the test cells are initially cycled to 50 cycles at 0.1 C and subsequently employed for high current rates. In the first cell, the C rate is increased from 0.1 to 1 C, the specific discharge capacity is decreased from 190 to 125 mAh g^{-1} and the capacity is maintained over 99% for 10 cycles. Such behavior is expected in high current rates, while cycling the cell at high C rates, the surface of active material only involves the reaction rather than bulk. When the C rate is switched back to 0.1 C, the capacity is retained from 120 to 190 mAh g^{-1}.

Similarly, in the duplicate cell, the C-rate is increased from 0.1 to 0.2 C, a small amount of capacity fading (from 175 to 165 mAh g^{-1}) is noted. With further increase in current to 0.5, 1 and 2 C rates, the cell delivered excellent discharge capacitive properties with negligible capacity fade. Finally, the current rate is relaxed to 0.1 C, and the discharge capacity is retained for its original state and maintained at 145 mAh g^{-1} for after 20 cycles. From the above analysis, it can be concluded that the V_2O_5 prepared at 600°C for 1 h by urea combustion shows good cell capabilities and capacity retention is maintained following cycling at higher C rates.

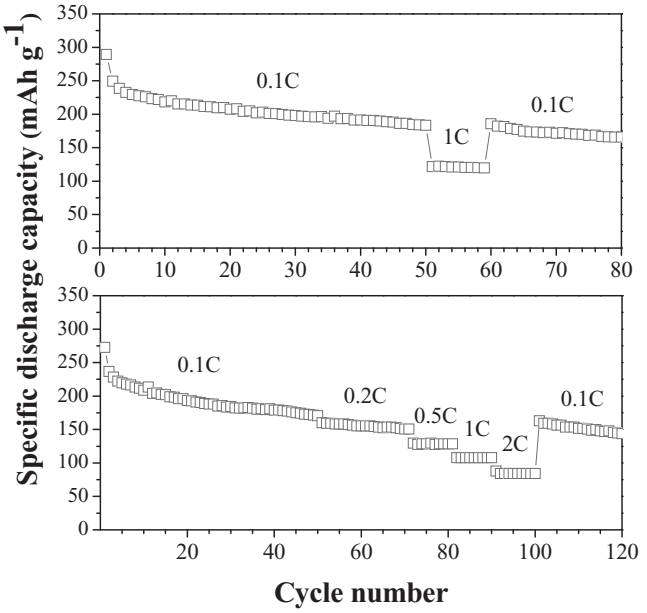

Figure 8. Rate capability studies of two duplicate cells comprising VUC 600-1 sub-micron size powders at room temperature.

Electrochemical impedance spectra (EIS) for various V_2O_5 powders are recorded in the frequency range 100 kHz to 5 mHz. The typical Nyquist ($-Z''$ vs. Z') plots for freshly made cells after stabilization of 24 h are shown in Figure 9. The cells mainly display semicircles in the high and middle frequency ranges and 45°C straight line in the low-frequency range, suggesting V_2O_5 electrode kinetics.[20,40] The Nyquist plots consist of two parts, a high-to-middle frequency semicircle and a sloping line to the real axis (Z') in the lower frequency range corresponds to Warburg-type element. Ionic diffusion from the bulk of electrolyte to the reaction sites affects impedance mostly at high frequencies. The high-to-middle frequency semicircle is related to the lithium-ion migration through electrode/electrolyte interphase and surface film capacitance,[41] and the sloping straight line at low frequency ranges corresponds to the dominant mass transport and is indicative of controlled diffusion of electro-active species across the interface between surface films in the V_2O_5 matrix; it also involves the capacitive effect of the conducting carbon.

To perform a quantitative analysis, a simple equivalent circuit is configured to simulate the EIS and shown in Figure 9c. The circuit parameters are calculated by using the series combination of R_s, R_{SEI+ct}//CPE_{SEI+dl}, R_b//CPE_b and W_o, the finite length Warburg resistance (open-circuit terminus). At high characteristic frequency, intercept of the semicircle extended to the Z' axis is reflected by an ohmic resistance (R_s), which includes resistance from separator and electrolyte solution. The R_{SEI+ct} is ascribed to resistance due to the lithium ion migration through the interface between the surface layer of the V_2O_5 cathode/electrolyte and surface film resistance.[20] CPE_{SEI+dl} correspond to the surface film and double-layer capacitance at the V_2O_5 electrode surface. The bulk resistance (R_b) arises due to combination of electronic resistivity of active material (V_2O_5) and ionic conductivity of electrolyte filled by the pores of the composite electrode (active material, conducting carbon and binder). The constant phase element CPE_b is the bulk capacitance arising due to the complicated electrochemical processes. The constant phase element is an empirical impedance function of the type, $CPE_{SEI+dl/b} = A(j\omega)^{-\alpha SEI+dl/b}$, replaced with capacitance by taking into account the rough nature of the electrode, where ω is the angular frequency, and A and $\alpha_{dl/b}$ are the constants. The degree of distortion of the impedance spectra can be obtained from the value of $\alpha_{SEI+dl/b}$.[40,42]

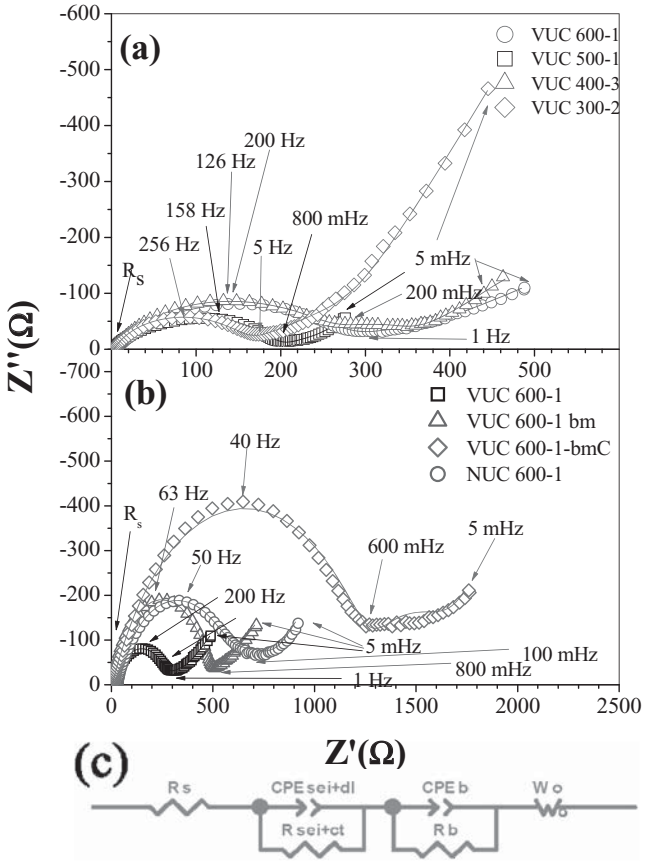

Figure 9. Nyquist plots of fresh cells (a) VUC 600-1, 500-1, 400-3 and 300-2, (b) VUC 600-1, ball-milled VUC 600-1, ball-milled VUC 600-1 with carbon and NUC 600-1 and (c) equivalent circuit model used. Symbols represent experimental spectra and lines indicate fitted data of above model.

The experimental data are subjected to a non-linear least square fitting procedure and equivalent circuit parameters are obtained for V_2O_5 cells after the same length of equilibration period. The values obtained from the fitting are presented in Table II. As seen in Figure 9a, VUC 600-1 shows a semicircle with a characteristic frequency of 200 Hz, whereas VUC 500-1 shows a semicircle with a characteristic frequency of 158 Hz. The characteristic frequencies for VUC 400-3 and VUC 300-2 are observed to be at 126 and 256 Hz respectively. The value R_{SEI+ct} is observed highest for VUC 600-1 sample (∼275 Ω), followed by VUC 400-3 (∼265 Ω), whereas for VUC 500-1 and VUC 300-2, the value of R_{SEI+ct} is found to be <10 Ω. Similarly, the highest capacitance CPE_{SEI+dl} is observed for 600-1 (∼32 μF) and lowest for VUC 300-2 (275 pF). The R_{SEI+ct} and CPE_{SEI+dl} values can be correlated to the available electro-active surface area facilitated by V_2O_5 cathode through in which charge transfer occurs. This clearly inferred that the difference in surface area affects the formation of surface film and charge transfer properties. The high R_{SEI+ct} and CPE_{SEI+dl} values of VUC 600-1 sample indicate the more active formation of surface films on the surface of the electrode. Consequentially, VUC 600-1 exhibited the lowest R_b value among the other samples, whereas it shows highest CPE_b value (∼10 mF). Due to lower bulk resistance (R_b), the cycling stability is certainly improved.[20] The Warburg diffusion resistance (W_o) is observed as maximum for VUC 600-1 (∼1.75 kΩ) and minimum for VUC 500-1 (∼208 Ω), which indicates VUC 500-1 is containing a lower number of available diffusion pathways when compared to the former.

Table II. Values for various samples obtained from fitting of EIS spectra.

Elements Sample	R_{SEI+ct} (Ω)	CPE_{SEI+dl} (μF)	R_b (Ω)	CPE_b (mF)	W_o (Ω)
VUC 300-2	1.177	2.75×10^{-8}	145.7	0.0249	359
VUC 400-3	265.4	35.3	74.65	2.99	700
VUC 500-1	8.301	0.615	160.3	0.0375	208
VUC 600-1	275.0	32.0	53.86	10.2	1750
VUC 600-1 ball-milled	443.7	13.8	45.67	5.07	0.0248
VUC 600-1 ball-milled with carbon	1276	17.2	323.5	5.32	0.00176
NUC 600-1	545.4	23.2	193.6	2.38	13900

EIS spectra were also recorded for ball-milled VUC 600-1 and directly sintered NUC 600-1 for comparison and presented in Figure 9b. For the ball-milled sample, reduction of particle size leads to increase in electro-active surface area, thus increasing the film formation. This can be seen from the increase in R_{SEI+ct} value and there is a slight decrease in CPE_{SEI+dl} (32 μF to 14 μF) is noted when compared to native compound. The R_b and CPE_b are also reduced to 46 Ω and 5 mF respectively, compared to VUC 600-1. This may be correlated to the decrease in the porosity of the ball-milled sample.[43] Similarly, Warburg resistance is also noticeably reduced from ∼1.75 kΩ to 25 mΩ. The decrease in Warburg impedance values indicate that diffusion pathways have been increased in the ball-milled sample due to the reduction in the particles size. Further ballmilling with conductive carbon (Super P Li) to the VUC 600-1 sample leads to the increase in R_{SEI+ct} and CPE_{SEI+dl} values to ∼1.30 kΩ and 17 μF respectively from ball milled powders. This is believed to be due to the capacitive effect of Super P Li carbon, in which ballmilling further enabled more homogeneous mixing of the active material and conductive species. The R_b is also increased to 323 Ω, however, there is no major variation in the CPE_b value (∼5 mF) upon addition of Super P Li carbon. The decrease in Warburg resistance to 1.7 mΩ indicates that the addition of conductive carbon leads to a faster diffusion of lithium ion during electrochemical reaction, which has been reflected in the cycling performance of the cells.

In addition to the above, the powder NUC 600-1 showed highest R_{SEI+ct} values (545 Ω) and capacitive effect of the interphase is reduced from 32 μF to 23 μF when compared to the combustion sample VUC 600-1. The bulk resistance is also increased to 194 Ω whereas bulk capacitance (CPE_b) is reduced to 2 mF. Finally, the high Warburg resistance (W_o) ∼13.9 kΩ indicated the large decrease in number of diffusion pathways, which results in poor performance during cycling.

From the EIS analysis, it can be concluded that larger particle size of VUC 600-1 enabled better cycling stability, though it exhibited slightly lower initial discharge capacity when compared to rest of the samples prepared at different conditions. Ball-milling is one of the approaches to reduce the particle size, which increases the contribution toward more robust surface film formation via larger available area. However, overall bulk resistivity is reduced when compared to VUC 600-1. Hence, ballmilling of V_2O_5 powder increases number of diffusion pathways for Li^+ ion transport, which is observed from the improved capacity retention properties. Moreover, urea combustion method provides improved the capacitive properties of V_2O_5 powders and also increased the electro-active surface which is reflected in the reduced Warburg resistance value when compared to that of non-combustion synthesized sample NUC 600-1. This result is also in good agreement with higher initial capacity and cycling profile observed for VUC 600-1 when compared to NUC 600-1.

Conclusions

Sub-micron size V_2O_5 particles are obtained via one-step urea combustion synthesis method and the parameters like sintering tem-

perature and duration has been optimized. FE-SEM showed the formation of particles in the range of 200–800 nm. The XRD pattern reveal the formation of single phase V_2O_5 particulates and FT-IR studies showed the complete removal of organic impurities during synthesis. Electrochemical studies are conducted in half-cell configurations and V_2O_5 synthesized at 600°C for 1 h delivered highest initial discharge capacity of 320 mAh g^{-1} among the rest and exhibited stable capacity at more than 70% retention after 50 charge-discharge cycles. The urea combustion synthesis also enables improved capacity and rate capabilities of V_2O_5. Electrochemical impedance studies bring about new insights to the kinetics of urea-combusted V_2O_5 and provided explanation for the cyclic retention properties of V_2O_5 during the Li intercalation/de-intercalation processes.

Acknowledgments

This work was supported by funding from the National Research Foundation, Clean Energy Research Project grant number NRF2009EWT-CERP001-036. Authors also acknowledge Timcal for gratis providing Super P™ Li Carbon black.

References

1. S. Fletcher, *Bottled Lightning: Superbatteries*, Electric Cars, and the New Lithium Economy Hill and Wang, New York (2011).
2. A. N. Jansen, A. J. Kahaian, K. D. Kepler, P. A. Nelson, K. Amine, D. W. Dees, D. R. Vissers, and M. M. Thackeray, *Journal of Power Sources*, **81**, 902 (1999).
3. O. K. Park, Y. Cho, S. Lee, H.-C. Yoo, H.-K. Song, and J. Cho, *Energy & Environmental Science*, **4**, 1621 (2011).
4. J. M. Tarascon, *Philosophical Transactions of the Royal Society a-Mathematical Physical and Engineering Sciences*, **368**, 3227 (2011).
5. B. Scrosati and J. Garche, *J. Pow Sources*, **195**, 2419 (2010).
6. T. Ohzuku and Y. Makimura, *Chem. Lett.*, **30**, 642 (2001).
7. D. Liu, Y. Liu, B. B. Garcia, Q. Zhang, A. Pan, Y.-H. Jeong, and G. Cao, *J. Mater. Chem.*, **19**, 8789 (2009).
8. T. Zhai, H. Liu, H. Li, X. Fang, M. Liao, L. Li, H. Zhou, Y. Koide, Y. Bando, and D. Golberg, *Adv. Mater.*, **22**, 2547 (2010).
9. Y.-S. Hu, X. Liu, J.-O. Müller, R. Schlögl, J. Maier, and D. S. Su, *Angewandte Chemie International Edition*, **48**, 210 (2009).
10. E. A. Olivetti, K. C. Avery, I. Taniguchi, D. R. Sadoway, and A. M. Mayes, *Journal of The Electrochemical Society*, **155**, A488 (2008).
11. Y. Wang and G. Cao, *Chemistry of Materials*, **18**, 2787 (2006).
12. C. Ban, N. A. Chernova, and M. S. Whittingham, *Electrochem. Comm.*, **11**, 522 (2009).
13. A. M. Glushenkov, M. F. Hassan, V. I. Stukachev, Z. Guo, H. K. Liu, G. G. kushinov, and Y. Chen, *J. Solid State Electrochem*, **14**, 1841 (2010).
14. L. Mai, L. Xu, C. Han, X. Yu, Y. Luo, S. Zhao, and Y. Zhao, *Nano Lett.*, **10**, 4750 (2010).
15. E. A. Ponzio, T. M. Benedetti, and R. M. Torresi, *Electrochim. Acta*, **52**, 4419 (2007).
16. P. Ragupathy, S. Shivakumara, H. N. Vasan, and N. Munichandraiah, *J. Phys. Chem. C*, **112**, 16700 (2008).
17. C. V. S. Reddy, S. S. A. Wicker, J. Edwin, H. Walker, Q. L. Williams, and R. R. Kalluru, *J. Electrochem. Soc.*, **155**, A599 (2008).
18. C. V. S. Reddy, J. Wei, Z. Quan-Yao, D. Zhi-Rong, C. Wen, S.-i. Mho, and R. R. Kalluru, *J. Power Sources*, **166**, 244 (2007).
19. X. Ren, Y. Jiang, P. Zhang, J. Liu, and Q. Zhang, *J. Sol-Gel Sci Technol*, **51**, 133 (2009).
20. Y. L. Cheah, N. Gupta, S. S. Pramana, V. Aravindan, G. Wee, and M. Srinivasan, *J. Power Sources*, **196**, 6465 (2011).
21. F. Huguenin, E. M. Girotto, R. M. Torresi, and D. A. Buttry, *J. Electroanalyt. Chem.*, **536**, 37 (2002).
22. C. V. S. Reddy, A.-P. Jin, X. Han, Q.-Y. Zhu, L.-Q. Mai, and W. Chen, *Electrochem. Comm.*, **8**, 279 (2006).
23. S. Suzuki, M. Hibino, and M. Miyayama, *J. Power Sources*, **124**, 513 (2003).
24. K. E. Swider-Lyons, C. T. Love, and D. R. Rolison, *Solid State Ionics*, **152-153**, 99 (2002).
25. Y. Sharma, N. Sharma, G. V. S. Rao, and B. V. R. Chowdari, *Electrochimica Acta*, **53**, 2380 (2008).
26. Y. Sharma, N. Sharma, G. V. S. Rao, and B. V. R. Chowdari, *Solid State Ionics*, **179**, 587 (2008).
27. E. I. Santiago, S. T. Amancio, P. R. Bueno, and L. O. S. Bulhoes, *Journal of Power Sources*, **97-8**, 447 (2001).
28. H. M. Rietveld, *Acta Crystallogr.*, **22**, 157 (1967).
29. H. M. Rietveld, *J. Appl. Crytallogr.*, **2**, 65 (1969).
30. R. W. Cheary and A. Coelho, *Journal of Applied Crystallography*, **25**, 109 (1992).
31. C. Navone, R. Baddour-Hadjean, J. P. Pereira-Ramos, and R. Salot, *Electrochim. Acta*, **53**, 3329 (2008).
32. C. Xiong, A. E. Aliev, B. Gnade, and K. J. Balkus Jr., *ACS Nano*, **2**, 293 (2008).
33. X. G. Jiang, C. Y. Li, Y. Chi, and J. H. Yan, *J. Hazard. Mater.*, **173**, 205 (2010).
34. G. Madhurambal, M. Mariappan, and S. C. Mojumdar, *Journal of Thermal Analysis and Calorimetry*, **100**, 763 (2010).
35. G. Madhurambal, M. Mariappan, and S. C. Mojumdar, *Journal of Thermal Analysis and Calorimetry*, **100**, 853 (2010).
36. A. Sakunthala, M. V. Reddy, S. Selvasekarapandian, B. V. R. Chowdari, and P. C. Selvin, *Energy Environ. Sci.*, **4**, 1712 (2011).
37. J. M. Cocciantelli, J. P. Doumerc, M. Pouchard, M. Broussely, and J. Labat, *J. Power Sources*, **34**, 103 (1991).
38. A. Q. Pan, J. G. Zhang, Z. M. Nie, G. Z. Cao, B. W. Arey, G. S. Li, S. Q. Liang, and J. Liu, *Journal of Materials Chemistry*, **20**, 9193 (2010).
39. S. Y. Zhan, C. Z. Wang, K. Nikolowski, H. Ehrenberg, G. Chen, and Y. J. Wei, *Solid State Ionics*, **180**, 1198 (2009).
40. S.-I. Pyun and J.-S. Bae, *Electrochim. Acta*, **41**, 919 (1996).
41. S. S. Zhang, K. Xu, and T. R. Jow, *Electrochim. Acta*, **49**, 1057 (2004).
42. C.-j. Cui, G.-m. Wu, B. Z. Jun Shen, Z.-h. Zhang, H.-y. Yang, and S.-f. She, *Electrochim. Acta*, **55**, 2536 (2010).
43. D. A. Semenenko, T. L. Kulova, A. M. Skundin, D. M. Itkis, E. A. Pomerantseva, E. A. Goodilin, and Y. D. Tretyakov, *Mendeleev Commun*, **20**, 12 (2010).
44. D. Yu, C. Chen, S. Xie, Y. Liu, K. Park, X. Zhou, Q. Zhang, J. Li, and G. Cao, *Energy Environ. Sci.*, **4**, 858 (2010).
45. S. Wang, Z. Lu, D. Wang, C. Li, C. Chen, and Y. Yiu, *J. Mater. Chem.*, **21**, 6365 (2011).
46. Y. P. Chen, G. Yang, Z. H. Zhang, X. Y. Yang, W. H. Hou, and J. J. Zhu, *Nanoscale*, **2**, 2131 (2010).
47. K. H. Kim, D. K. Roh, I. K. Song, B. C. Lee, and S. H. Baeck, *Journal of Solid State Electrochemistry*, **14**, 1801 (2010).
48. C. Ban and M. S. Whittingham, *Solid State Ionics*, **179**, 1721 (2008).
49. D. Zhu, H. Liu, L. Lv, Y. D. Yao, and W. Z. Yang, *Scripta Materialia*, **59**, 642 (2008).
50. X. Li, W. Li, H. Ma, and J. Chen, *J. Electrochem. Soc*, **154**, A39 (2007).
51. C. Wu and Y. Xie, *Energy Environ. Sci.*, **3**, 1191 (2010).